ChemPubSoc Europe

DOI: 10.1002/cplu.201402388

CHEMPLUSCHEM Full Papers

Preparation, Surface and Crystal Structure, Band Energetics, Optoelectronic, and Photocatalytic Properties of $Au_xCd_{1-x}S$ Nanorods

Rohit Singh and Bonamali Pal*[a]

A series of novel $Au_xCd_{1-x}S$ materials ($x=0$, 0.01, 0.02, 0.03, 0.05, 0.07, 0.1) were prepared and their optical properties, structural-surface morphology, and photocatalytic activity for oxidation and reduction reactions under visible-light irradiation were studied. X-ray diffraction confirmed the shrinkage of the hexagonal crystal structure of CdS; the lattice parameters decreased as $a=4.190\rightarrow4.072$ Å and $b=c=6.790\rightarrow6.635$ Å with increased loading (1–10 mol%) of the Au^{3+} dopant. Optical spectra of $Au_xCd_{1-x}S$ revealed a significant red-shift (485→538 nm) of the absorption onset and band edge emission (506→530 nm) with notable quenching in photoluminescence. The bandgap energy decreases (2.71→2.41 eV) with increasing Au^{3+} doping of the CdS nanorods along with considerable shifting of valence band (+1.13→+1.04 eV) and conduction band positions (−1.58→−1.36 eV) versus NHE. The surface area of bare CdS (90.56 m^2g^{-1}) is gradually reduced to 12.32 m^2g^{-1} with increasing Au^{3+} doping content. The photocatalytic activity considerably improves with doping, where the $Au_{0.1}Cd_{0.9}S$ composite displays the highest levels of photooxidation (95%) of 0.5 mM salicyldehyde and reduction of 5 mM *m*-dinitrobenzene to *m*-nitroaniline (44%) and *m*-phenylenediamine (52%) relative to bare CdS (50%) probably due to the homogeneous dispersion of Au^{3+} ions throughout CdS crystal, their superior band-energetics for facile charge-separation and better photostability.

Introduction

Recently, anisotropic nanocrystals (NC) such as nanorods (NR) and nanowires (NW) have attracted widespread attention.[1–5] In contrast to conventional spherical nanoparticles, in these materials many beneficial physicochemical properties[6–11] can be improved owing to the availability of different atomic planes on crystal facets, the two-dimensional quantum confinement effect, their larger per-particle surface area, high diffusion of charge carriers, length to diameter controlled absorption and emission, and extended lifetime of photogenerated charge carriers. In this context, metallic or semiconducting nanostructures with different anisotropies have been broadly studied[12–14] for photovoltaic applications and for the photocatalytic production of hydrogen and degradation of toxic pollutants. It is well proven that the activity of a semiconductor (SC) can be further improved by modifying its surface with metal nanoparticles (NPs). The free electrons will transfer from the semiconductor to the metal (M) side (if $\varphi_m > \varphi_s$) until their Fermi levels are aligned by generation of a Schottky barrier through the M–SC interface.[15–17] As a result, various nanocomposites such as Cu/ZnO, Au/CeO_2, Pt/CdS, Au/ZnO, and sulfur/graphene (S/GR) have been studied[16–21] to improve charge separation for facile photophysical and chemical properties. It has been well-accepted that photoactivity is highly dependent upon the size distribution of the deposited metal particles, and the interfacial contact area and nature of metal–support interactions. Conventional metal deposition techniques lead to uncontrolled and irregular size distribution of metal particles onto the SC surface[13,22,23] that have a poor electrical contact, that is, M-NPs are present only on the surface and not at all uniformly throughout the crystal. Moreover, the higher amount of metal ions present would act as recombination centers for e^-/h^+ pairs[24] through the process described by Equation (1).

$$M^{n+} + n e^-_{CB} \rightarrow M^{0+} \quad (1)$$

Before recombination, e^-/h^+ pairs are well separated by a large electric field within the space charge region. But when the metal concentration increases, this region becomes narrower and the depth of light that can penetrate the SC extends beyond the space charge region. As a result, the recombination of photogenerated e^-/h^+ pairs in the SC increases as there is no driving force to separate them. This means that improvement in photoactivity is always governed by the number of metal particles deposited in the semiconductor and not by their loading. In contrast, metal ion doping is believed to improve the physicochemical properties because it can lead to a shift of band edge levels that drive oxidation and reduction reactions. The creation of doping levels results in the narrow-

[a] R. Singh, Dr. B. Pal
School of Chemistry and Biochemistry
Thapar University
Patiala, Punjab 147 004 (India)
Fax: (+91) 175-2364498
E-mail: bpal@thapar.edu

Supporting information for this article (including preparation of Au^{3+}-doped CdS/TiO_2 solar cells, EDS and MP-AES analysis, absorption spectra, summary of various physical properties of $Au_xCd_{1-x}S$ sample, and GC-MS traces) is available on the WWW under http://dx.doi.org/10.1002/cplu.201402388.

ing of the band gap for higher visible spectral response, suitable stable structures, homogeneous distribution of charge, and more importantly the improvement of ionic bond formation.

Cadmium sulfide (CdS), a visible-light-driven photocatalyst having band gap of roughly 2.4 eV and suitable negative flat-band potential, is a promising material. However, some shortcomings, such as quick recombination of photogenerated charge carriers and photodissolution during the photocatalytic reaction in aqueous medium, have restricted its practical application. Literature reports[25–27] revealed that the intentional incorporation of M^{n+} ions into crystal lattices by replacing some Cd^{2+} ions led to a homogeneous dispersion of $M^{n+}{}_xCd_{1-x}S$ junctions throughout the crystal, which is believed to result in better ohmic contact relative to that of M-CdS composites made by deposition (see Scheme 1). To address this, various Mn^{2+}-, Cu^{2+}-, Ni^{2+}-, and In^{3+}-doped CdS nanoparticles were studied[28–31] in order to improve visible response and enhance photocatalytic activity, durability, and efficiency in solar cells. However, the doping of Au^{3+} into CdS-NR has not been investigated despite their comparable dimensions (Au^{3+} = 0.85 Å, Cd^{2+} = 0.97 Å),

Well-matched bands energetics,[32,33] quick Fermi level equilibration, and the homogeneous dispersion of Au^{3+} ions into the elongated CdS-NR crystal were expected due to the better diffusion of charge carriers along the crystallographic *c*-axis. The doping of Au^{3+} at different concentration levels into CdS-NR was presumed to result in a change in the conduction band and valence band edge positions, which facilitates the transfer of e^- and h^+ for corresponding reduction and oxidation processes. Moreover, Au^{3+} doping into CdS-NR imparts extra charge and creates more defects sites in the CdS crystal, which may help in effective separation and migration of the photoexcited charge species for improved photocatalytic properties.

Thus, in the present study, $Au_xCd_{1-x}S$ (x = 0, 0.01, 0.02, 0.03, 0.05, 0.07, 0.1) nanorod composites were prepared in order to study the modified optoelectronic properties, band gap energy, band positions, surface and structural changes, current–voltage characteristics, and photocatalytic activity for the model oxidation and reduction reactions under sunlight irradiation.

Results and Discussion

Structural and morphological analysis

Figure 1 shows X-ray diffraction peaks of $Au_xCd_{1-x}S$ (x = 0, 0.01, 0.02, 0.03, 0.05, 0.07, 0.1) composites having characteristics of the hexagonal phase of the wurtzite crystal structure (JCPDS No. 41-1049). No peaks of any other segregated phases (Au^{3+} or AuS) or impurities were detected even at 10 mol% loading, indicated the effective doping of Au^{3+} into the CdS hexagonal crystal. The relatively intense (002) diffraction peak indicates that the CdS-NR have grown along the crystallographic *c*-axis.

Figure 1b (enlarged view; 2θ = 22–32°) shows that the peak positions of the (100), (002), and (101) planes are slightly red-shifted with the increase in Cd^{2+}/Au^{3+} molar ratio. The 2θ value along the (002) diffraction plane exhibits a red-shift from 26.217° to 26.844° with increasing loading of Au^{3+} (0→

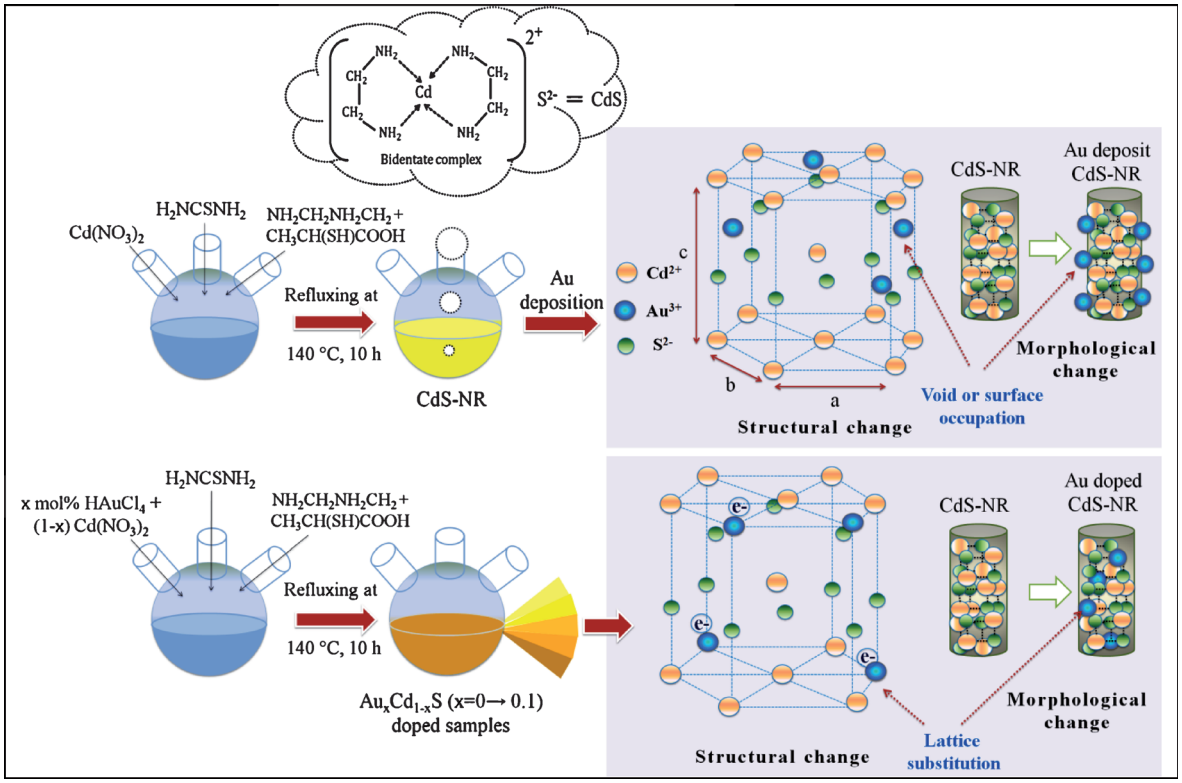

Scheme 1. Schematic representation of structural and morphological difference in CdS nanorods after Au^{3+} doping and deposition.

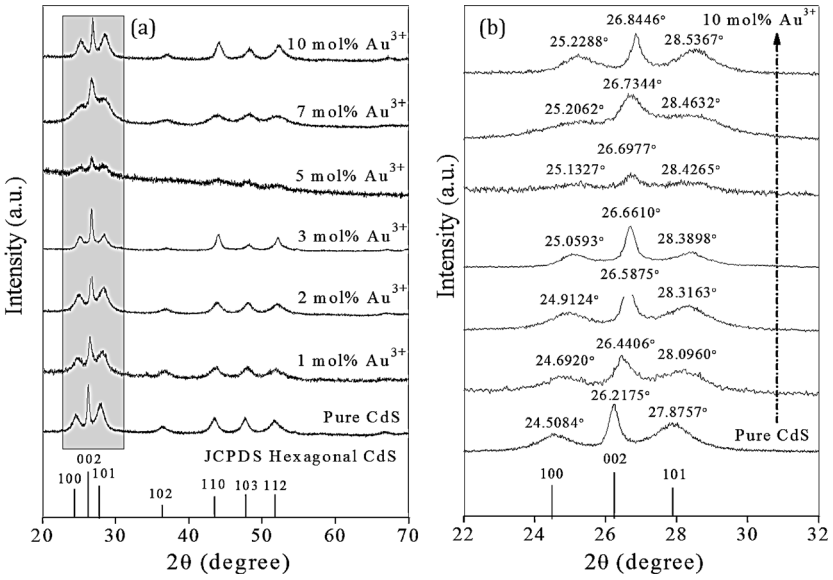

Figure 1. a) XRD patterns of $Au_xCd_{1-x}S$ samples ($x = 0$, 0.01, 0.02, 0.03, 0.05, 0.07, 0.1) and b) an enlarged view of the peaks corresponding to the (100), (002), and (101) crystal planes.

10 mol%), which is quite reasonable because the ionic radius of Cd^{2+} (0.97 Å) is larger than that of Au^{3+} (0.85 Å).

The lattice constants ($a = 4.190 \rightarrow 4.072$ Å and $b = c = 6.790 \rightarrow 6.635$ Å) were found to decrease with increasing Au^{3+} loading, indicating the replacement of Cd^{2+} ions with Au^{3+}. The exponential behavior of the lattice constants of CdS-NR with increasing Au^{3+} loading is shown in Figure 2. These results are not in line with Vegard's law,[34] which indicates a linear relationship between the lattice constants and the dopant concentration for a homogeneous solid solution. Therefore, it is presumed that there is an optimum level of Au^{3+} doping into CdS crystal, above which it will no longer behave as a solid solution.

High-resolution transmission electron microscopy (HRTEM) and energy-dispersive X-ray spectroscopy (EDS) analysis have been carried out to elucidate the size, shape, crystallinity, lattice interplaner distance, and elemental composition of bare

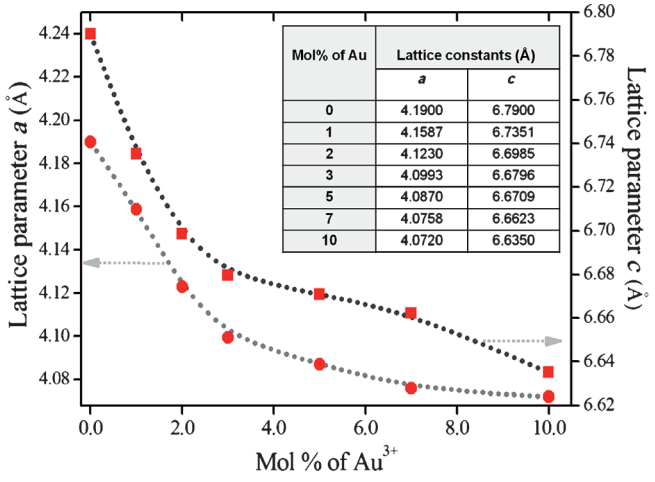

Figure 2. Variation of lattice parameters with increasing Au^{3+} doping into the CdS-NR crystal structure.

and doped samples. As shown in Figure 3, CdS particles are found to have a rodlike shape with a diameter of about 5–10 nm and a length of 100–200 nm. These nanorods are well dispersed and do not display morphological changes even after the doping of 2 and 5 mol% Au^{3+} into CdS lattices. The interplaner distance notably increases $0.34 < 0.39 < 0.45$ nm for the bare, 2 mol% and 5 mol% Au^{3+}-doped CdS-NR, respectively, which completely agrees with their profile of frame at different portions of the image and might be due to differences in their ionic radii. EDS analysis also confirms the presence of Cd, S, and Au in the $Au_xCd_{1-x}S$ nanostructure. Au was found to be present in reasonable loadings: 0.70, 2.88, 6.40, and 8.88 atom% for the 1, 3, 7, and 10 mol% Au^{3+}-doped CdS samples (SI-Figure 1). Furthermore, the microwave plasma atomic emission spectrometry (MP-AES) analysis revealed 0.28, 2.54, 5.29, and 6.69% of Au in 1, 2, 5 and 7 mol% Au^{3+}-doped CdS samples, respectively (SI-Figure 2).

The surface area (Table S1) of bare CdS-NR (90.56 $m^2 g^{-1}$) significantly decreased to 12.32 $m^2 g^{-1}$ after increasing levels of Au^{3+} incorporation, which might be attributed to the partial filling of pores in the CdS nanocrystals and surface morphological changes.

Optical study

The absorbance of CdS-NR (SI-Figure 3) is significant red-shifted (485 → 538 nm) with an increase upon Au^{3+} doping. Clearly, CdS-NR formed in the absence of thiol groups exhibited absorbance around 510–515 nm (not shown here), which indicates the role of a stabilizing agent in providing less agglomerated nanoparticles. Interestingly, $Au_xCd_{1-x}S$ samples do not exhibit any characteristic surface plasmon band (SPR) despite having a high loading of Au^{3+} probably due to the mixing of electronic states at the Au^{3+}–CdS interface. This is consistent with previous reports[25,35] which explain that in this type of strong composites the boundary effect of Au is significantly reduced due to the delocalization of plasma electrons into the CdS portion and therefore the exciton as well as the plasmon band is suppressed. The above results show that the absorption spectrum is broadened by the doping of Au^{3+}; this indicates that doped samples have greater carrier concentration.

Figure 4a shows that the band gap energies decrease (2.71 → 2.41 eV) with increasing Au^{3+} doping in the $Au_xCd_{1-x}S$ composites. The increase in the Au^{3+} doping level in CdS-NR results in the narrowing of energy band positions, which indicates that the as-synthesized doped samples are adducts but

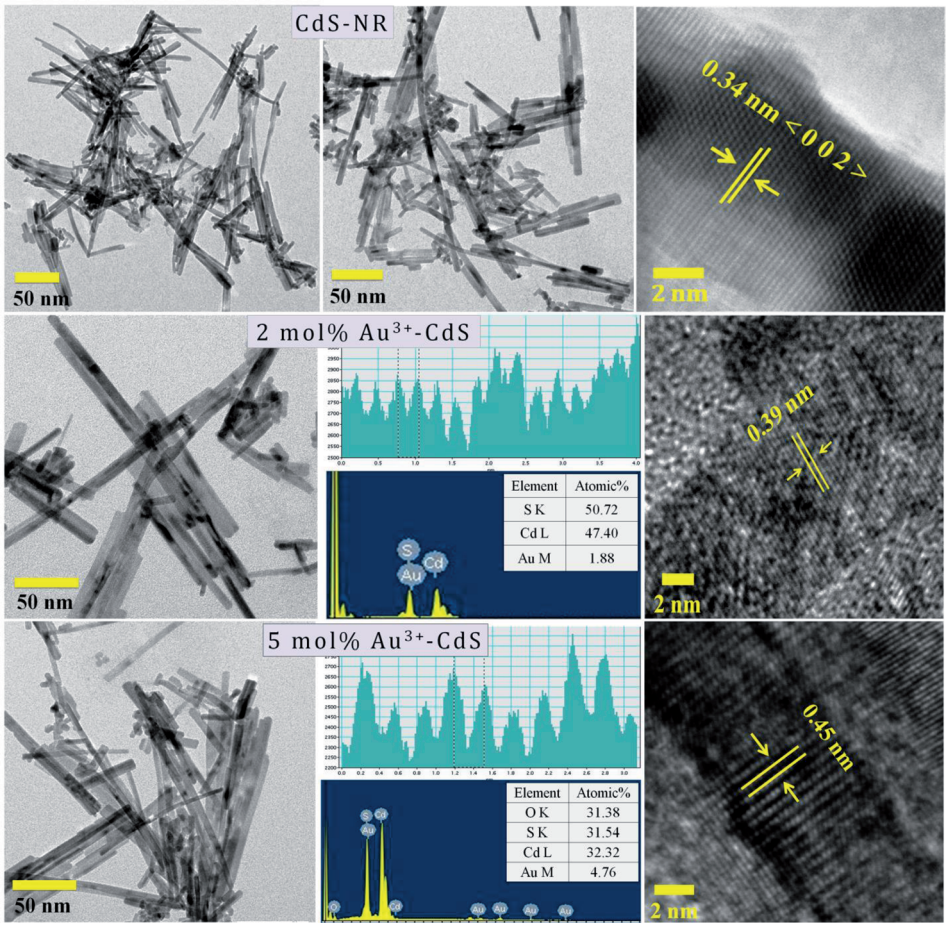

Figure 3. HRTEM images of pure and Au^{3+}-doped CdS nanoparticles, their lattice interplaner distances, profile of frame for the average fringe width, and energy-dispersive X-ray spectra.

substituted products. The was further supported by their variation in color from light yellow to golden yellow (Figure 4b) relative to the light yellow color of bare CdS-NR.

The band edge positions of various $Au_xCd_{1-x}S$ samples were calculated as a function of their band gap energies (Figure 5). To determine the conduction band (CB) edge positions in relation to the normal hydrogen electrode potential (NHE), Equation (2) [34,36] was employed.

$$E_{CB} = X - E^e - 0.5E_g \quad (2)$$

Here E_{CB} is the conduction band potential, X is the electronegativity of a semiconductor, and is defined as the arithmetic mean of the first ionization energy and electron affinity, E^e is the energy of free electrons on the hydrogen scale and that is equal to 4.5 eV, and E_g is band gap energy of a given semiconductor. The CB positions were found to decrease from −1.58 to −1.36 eV with increasing value of *x* in $Au_xCd_{1-x}S$ ($x = 0$, 0.01, 0.02, 0.03, 0.05, 0.07, 0.1).The valence band (VB) edge positions determined by using Equation (3)

$$E_{VB} = E_{CB} + E_g \quad (3)$$

are found to decrease from +1.13 to 1.04 eV with increasing *x* content in $Au_xCd_{1-x}S$ samples. The band structure model suggests that band gap positions of various doped samples can be adjusted continuously by changing the Au^{3+}/Cd^{2+} ratio in $Au_xCd_{1-x}S$ nanostructures.

The change in the photoluminescence (PL) emission spectra of CdS-NR with an increase in Au^{3+} loading on excitation at 380 nm in ethanol suspension (1 mg mL^{-1}) is shown in Figure 6a. In general, PL originates either from the band edge that is, due to the recombination of e^-/h^+ pairs or surface defects i.e., the radiative recombination of trapped charge carriers at the defect sites. Au^{3+} doping at increasing concentration levels in CdS-NR resulted in a slight red-shift (505→512 nm) in the band edge emission and higher luminescence quenching. The introduction of Au^{3+} into CdS structure by replacing some Cd^{2+} ions facilitates higher separation of charge by the shuttling of photogenerated electrons. The delocalization of charge carriers is extended which prevents their recombination. It is assumed from PL spectra of doped samples that some defect states are generated near the highest occupied VB level prior to recombination of charge carrier (see Figure 6b).

Photochemical activity

Current–voltage (I–V) characteristics

As a significant change in the band edge positions in $Au_xCd_{1-x}S$ nanostructures has been observed, it is very interesting to study the *I–V* characteristics of bare and doped sample to explore their plausible change upon changes in the charge carrier concentrations. As shown in Figure 7, ruthenium-based N719 dye sensitized CdS-NR on a TiO_2 support gives a short circuit current of $J_{sc} = 0.270$ mA cm^{-2}, an open circuit voltage of $V_{oc} = 23.9$ mW), a fill factor of 0.283, and an efficiency η of 1.82×10^{-3}%. This trend is somewhat improved in 10 mol% Au^{3+}-doped CdS-NR with *Jsc* = 0.552 mA cm^{-2}, $V_{oc} = 47.4$ mW, a fill factor of 0.246, and an efficiency η of 6.46×10^{-3}%. Though the efficiency of the bare and doped samples is not satisfactory, the minute difference in the efficiency of $Au_xCd_{1-x}S$ nanostructure justifies the role of the metal dopant in prevent-

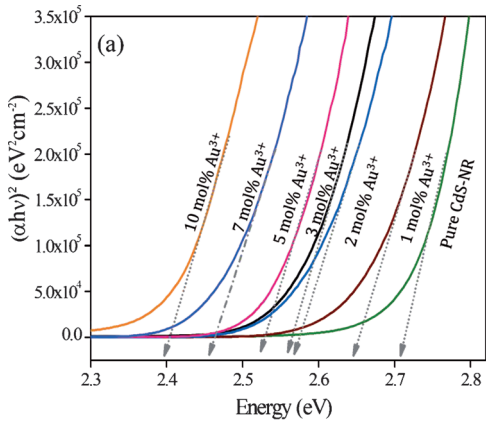

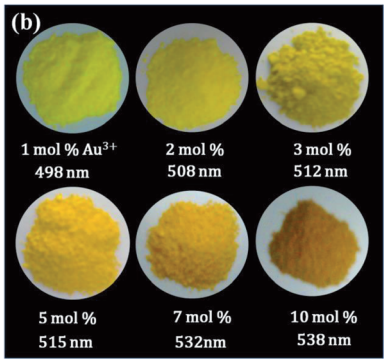

Figure 4. a) Band gap energy plots and b) colors of various $Au_xCd_{1-x}S$ samples ($x = 0$, 0.01, 0.02, 0.03, 0.05, 0.07, 0.1).

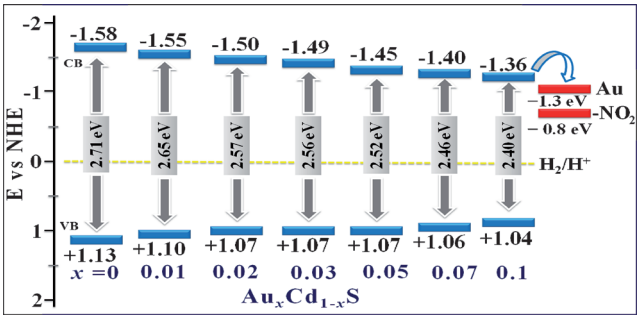

Figure 5. Variation of conduction and valence band edge position of various $Au_xCd_{1-x}S$ samples ($x = 0$, 0.01, 0.02, 0.03, 0.05, 0.07, 0.1) samples.

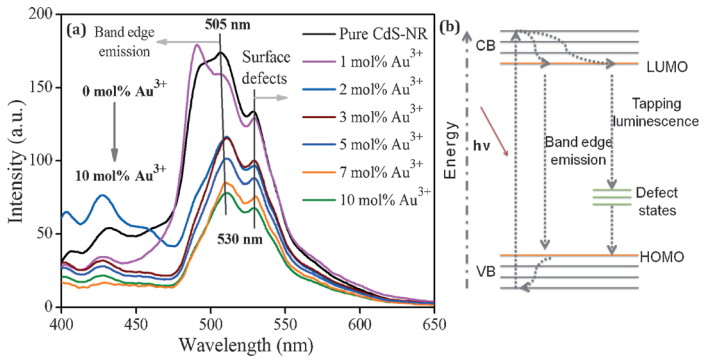

Figure 6. a) Change in photoluminescence (PL) spectra of CdS-NR with increasing levels of Au^{3+} doping. b) Proposed diagram for luminescence in doped samples.

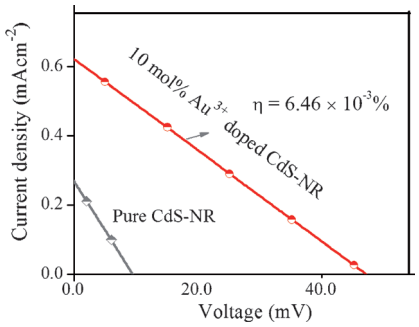

Figure 7. a) Current density–voltage characteristics for bare and 10 mol% Au^{3+}-doped CdS-NR.

ing charge recombination and increasing the light absorption/harvesting capacity.

As shown in Figure 8A, an exponential decrease in the concentration (C/C_o) of salicyldehyde was observed in the presence of bare and various doped $Au_xCd_{1-x}S$ samples; this was alsoevident from the change in the absorbance spectra (SI-Figure 4) during salicyldehyde photooxidation under sunlight irradiation. The photooxidation (%) was found to improve from 58 to 95% for the 1 and 10 mol% Au-doped samples, respectively, after 3 h of light exposure. This observed trend can be explained on the basis of the shift in VB edge positions for facile charge separation and decrease in band gap energies which may favor the harvesting of excitation energy and the homogeneous dispersion of Au^{3+}-CdS junctions for better Fermi level equilibration in $Au_xCd_{1-x}S$ samples. It seen in Figure 8B that a linear increase in CO_2 evolution is noticed in the first 2 h and a steady rate is found thereafter. The CO_2 production after 3 h exposure to sunlight was found to increase from 22% to 50% for the 10 mol% doped CdS-NR relative to pure CdS-NR.

Photoreduction of m*-dinitrobenzene (m-DNB)*

The influence of the change in CB positions of CdS-NR at increasing Au^{3+} doping levels on its reduction ability was investigated with the photoreduction of *m*-dinitrobenzene (5 mM) under sunlight irradiation. The photocatalytic activity notably improved with increasing Au^{3+} loading where $Au_xCd_{1-x}S$ ($x =$ 0.1) composites displayed the highest reduction (92%) of 5 mM *m*-dinitrobenzene to *m*-nitroaniline (yield = 44%) and *m*-phenylenediamine (yield = 52%). Figure 9 shows a plot of μmol of *m*-DNB consumed with time and the amount of *m*-NA and *m*-PDA products formed. The product distribution was studied by GC-MS analysis (SI-Figure 5), which confirmed the presence of *m*-DNB, *m*-NA, and *m*-PDA at retention times 17.6, 16.8, and 13.5 min, respectively, during 5 h reaction.

The fact that the photoefficiencies improve with increasing Au^{3+} doping content in the $Au_xCd_{1-x}S$ crystal can be well explained on the basis of a symmetric distribution of Au^{3+}–CdS interfaces, which results in better separation of charge carriers. The

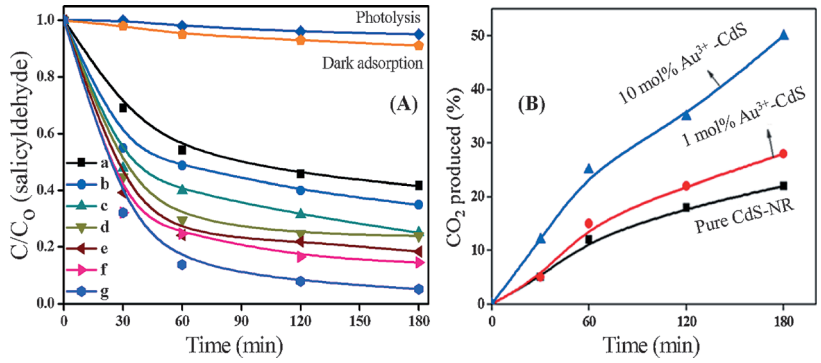

Figure 8. A) Plot of the time course of photooxidation of salicyldehyde (0.5 mM) under sunlight irradiation over a) CdS and Au^{3+}-doped CdS nanorods at dopant levels of b) 1 mol%, c) 2 mol%, d) 3 mol%, e) 5 mol%, f) 7 mol%, g) 10 mol%. B) CO_2 evolution (%) in the presence of various bare and Au^{3+}-doped CdS samples.

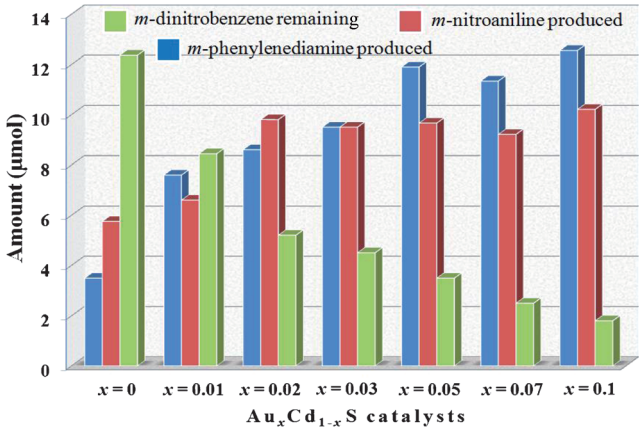

Figure 9. Photocatalytic efficiency for *m*-DNB (5 mM) reduction by various $Au_xCd_{1-x}S$ samples ($x = 0$, 0.01, 0.02, 0.03, 0.05, 0.07, 0.1) after 5 h of sunlight irradiation.

doping of Au^{3+} ions into the CdS matrix imparts extra negative charge to the crystal, which results in its higher reduction ability. More importantly, the change in CB edge positions from −1.58→−1.36 eV results in facile charge transfer to reaction species ($-NO_2$), whose reduction potential (−0.8 eV) lies much closer to that of the 10 mol% Au^{3+}-doped CdS sample. Also, the conduction band minimum of CdS at −1.36 eV is more negative than the Fermi level of Au (−1.3 eV on NHE scale).[37,38] Therefore, in the Au/CdS system, better Fermi level equilibration takes place, which results in suppression of the recombination of charge carriers and makes them available for corresponding reduction and oxidation processes.

It is well known that CdS often decomposes during a photochemical reaction, which deteriorates its activity.[39] As shown in Figure 10 for the salicyldehyde photo-oxidation in the presence of bare CdS-NR, catalyst degradation on the order of 21% was recorded after five repeated cycles due to its photochemical dissolution upon light irradiation. In contrast, the 10 mol% Au^{3-} doped CdS-NR effectively photodegraded the salicyldehyde without any significant deactivation even after a similar recycling process, which indicates its higher stability and activity; only a slight decrease (4%) in photoefficiency is noticed after five cycles. Any change in the surface structural morphology of bare and 10 mol% Au^{3+}-doped CdS-NR is further confirmed by XRD diffraction (Figure 10, bottom) pattern before and after successive cycles of salicyldehyde photodegradation under sunlight.

The intensity of all diffraction peaks for bare CdS-NR (especially for the (002) plane) is notably decreased and becomes broad due to partial dissolution of CdS after five successive cycles, whereas no such changes in the XRD pattern of 10 mol% Au^{3+}-doped CdS-NR are observed after the photoreaction under same conditions. Thus, it revealed that the Au^{3+}-doped CdS sample exhibits excellent stability and does not decompose or photocorrode during the photocatalytic reaction.

As evident from the comparative graph of surface area, lattice constant *c*, and photoactivity (Figure 11) an increase in the doping level (or mol%) of Au^{3+} in CdS (up to 10 mol%) resulted in a decrease in its surface area and lattice constant and an increases in its photooxidation and -reduction ability(%). This inverse surface area/photoactivity relationship leads us to con-

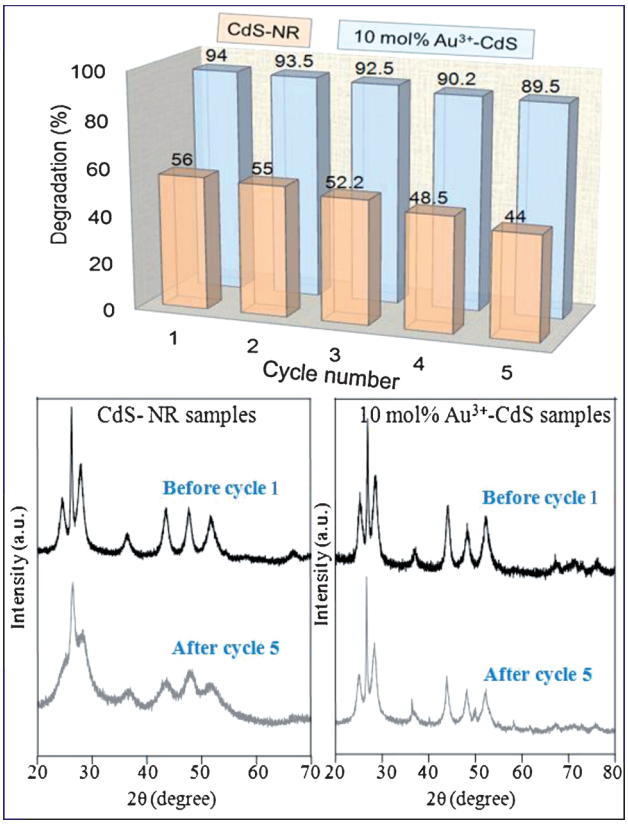

Figure 10. Photocatalytic activity and stability during reaction cycles with bare and 10 mol% Au^{3+}-doped CdS-NR for degradation of salicyldehyde (0.5 mM, 100 mL, 0.2 g) under 3 h of sunlight irradiation and the relative change in XRD patterns.

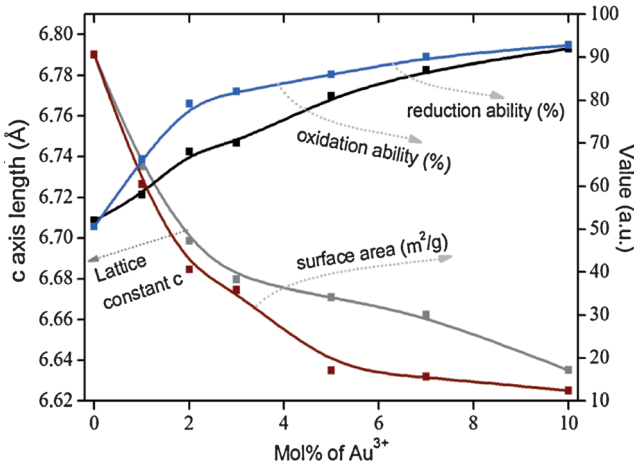

Figure 11. Correlation of lattice constant *c*, surface area, and photoredox ability of various Au^{3+}-doped CdS-NR catalysts.

clude that the role of metal as a co-catalyst in the photoseparation of charge carriers helps in decreasing recombination probability by prolonging the lifetime and the symmetric distribution of charge carriers; this is attributed to the improvement of ionic bond formation which dominates over their surface. The substitution of Cd^{2+} by Au^{3+}, that is, replacing an ion of a lower valence state (+2) with an ion of a higher valence (+3) state, imparts an extra charge in the process ($Cd^{2+} = Au^{3+} + e^-$) and is responsible for the higher number of electrons in the reaction for photoreduction purposes.

Conclusion

In summary, it is demonstrated that the manipulation of surface structure, optical absorption and emission, photocatalytic activity, and stability of CdS-NR could be controlled by the doping content (1–10 mol%) of Au^{3+} ions, which might not be possible for conventional Au/CdS nanocomposites made by other deposition techniques. These modified physicochemical properties were attributed to the charge separation ability upon photoexcitation, uniform dispersion of Au^{3+} ions, surface structural distortion, extra electrons imparted, and band edge potentials suitable for ready charge transfer to reactant species.

Experimental Section

Materials and methods

Cadmium nitrate tetrahydrate ($Cd(NO_3)_2{\cdot}4H_2O$), ethylenediamine ($H_2NCH_2CH_2NH_2$), thiourea ($SC(NH_2)_2$), hydrogen tetrachloroaurate(III) hydrate ($HAuCl_4.xH_2O$), *m*-dinitrobenzene ($C_6H_4N_2O_2$), *m*-phenylenediamine ($C_6H_8N_2O_2$), *m*-nitroaniline ($C_6H_4N_2O_2$), 3-mercaptopropionic acid ($C_3H_6O_2S$), salicyldehyde ($C_7H_6O_2$), and isopropanol (C_6H_8O) were purchased from Loba Chemicals and used without further purification. Deionized water was obtained using an ultrafiltration system (Milli-Q, Milipore) with a measured conductivity 35 mho cm^{-1} at 25 °C.

In a typical procedure,[40] (0.4−*x*) mmol $Cd(NO_3){\cdot}4H_2O$ and *x* mmol of $HAuCl_4{\cdot}xH_2O$ were mixed thoroughly in 10 mL of ethylenediamine prior to the addition of thiourea (0.8 mmol) and refluxed at 140 °C for 10 h. The products were obtained by centrifugation, and were washed with distilled water and ethanol and then dried at 60 °C for 1 h.

Characterizations

The optical properties were studied with a UV/Vis absorption (Analytikjena specord-205) spectrophotometer, diffused reflectance spectrophotometer (Avantes AvaSpec), and spectrofluorimeter (PerkinElmer LS55). The bandgap energy of various samples was evaluated by using the Tauc relation, which is given by $\alpha h\nu = A(h\nu - E_g)^{1/2}$ where A is a constant, E_g is the bandgap of the material, α is the absorption coefficient of the material, *h* is the Planck constant, and ν is the frequency of light. The exact value of the bandgap is estimated by extrapolating the straight-line portion of $(\alpha h\nu)^2$ versus E_g to the *x*-axis. The surface and structural properties were studied on a high-resolution transmission electron microscope (HRTEM, FEI Technai G2 F20 operated at 200 keV with resolution of 0.2 Å) and an X-ray diffractometer (PANalytical X'Pert PRO with Cu-Kα (k = 1.54060 Å). Energy-dispersive X-ray (EDS) spectroscopy was carried out on JEOL JSM-6510LB for elemental analysis. Microwave plasma atomic emission spectrometry (Agilent Technologies 4100, MP-AES) was used for quantitative analysis of Au in doped CdS samples. The Brunauer–Emmett–Teller (BET) specific surface area was carried out on single-point smartsorb 92/93 using N_2 adsorption method after preheating 100 mg of the sample at 150 °C for 1 h (N_2/He 70:30, as calibration gases) at cryogenic temperature. Related information on photocurrent–voltage measurements of pure and doped samples is given briefly in the Supporting Information.

Photocatalytic study

The photocatalytic activity was evaluated for the oxidation of 5 mL salicyldehyde (0.5 mM) in water and reduction (under argon atmosphere) of *m*-dinitrobenzene (5 mM, 25 μmol) in a test tube containing 50 % isopropanol and 10 mg of $Au_xCd_{1-x}S$ catalysts under sunlight irradiation (40–50 mW cm^{-2}). The reaction samples (after filtration through a 0.22 μm cellulose filter) were analyzed by UV/Vis spectrophotometry and high-performance liquid chromatography (HPLC, Agilent 1120 Compact LC) using a C-18 column and MeOH/H_2O (70:30) as a mobile phase at with detection at $\lambda = 254$ nm and a flow rate of 1 mL min^{-1}. Gas chromatography coupled with mass spectroscopy (GC-MS, Shimadzu, GC-2010 and GC-MS-QP 2010 plus with RTX-5Sil-MS column (15 m × 0.25 mm × 0.25 μm) of reaction samples was carried out in methanol solvent after extraction with dichloromethane. The CO_2 evolution was determined by gas chromatography (GC, NUCON-5765 equipped with a thermal conductivity detector (TCD)) by injecting a 1 mL gas sample into a Propak-Q column with a nitrogen gas flow (30 mL min^{-1}). All the physical properties of bare and doped samples are summarized in Table 1 in the Supporting Information.

Acknowledgements

This study was supported by a grant from the Department of Science and Technology (DST), India (Sanction order no. SR/NM/NS-40/2008) with partial financial support from the Rajiv Gandhi Na-

tional Fellowship (Sanction order no. F-16–1886(SC)/2010(SA-III)) by Ministry of Social Justice and Empowerment, India. We would like to acknowledge Sophisticated Analytical Instruments Laboratories (SAI), Thapar University for access to analytical facilities.

Keywords: CdS nanostructures · band energetics · crystal phase distortion · doping · photocatalysis

[1] C. J. Murphy, N. R. Jana, *Adv. Mater.* **2002**, *14*, 80 – 82.
[2] S. H. Kang, S. H. Choi, M. S. Kang, J. Y. Kim, H. S. Kim, T. Hyeon, Y. E. Sung, *Adv. Mater.* **2008**, *20*, 54 – 58.
[3] D. Katz, T. Wizansky, O. Millo, E. Rothenberg, T. Mokari, U. Banin, *Phys. Rev. Lett.* **2002**, *89*, 086801.
[4] A. Sitt, A. Salant, G. Menagen, U. Banin, *Nano Lett.* **2011**, *11*, 2054 – 2060.
[5] R. Singh, B. Pal, *Mater. Res. Bull.* **2013**, *48*, 1403 – 1410.
[6] B. Roldan Cuenya, *Acc. Chem. Res.* **2013**, *46*, 1682 – 1691.
[7] H. Kim, K. Yong, *ACS Appl. Mater. Interfaces* **2013**, *5*, 13258 – 13264.
[8] L. Li, C. Nan, Q. Peng, Y. Li, *Chem. Eur. J.* **2012**, *18*, 10491 – 10496.
[9] Z. Li, W. Wang, N. C. Greenhama, C. R. McNeill, *Phys. Chem. Chem. Phys.* **2014**, *16*, 25684.
[10] X. G. Peng, L. Manna, W. D. Yang, J. Wickham, E. Scher, A. Kadavanich, A. P. Alivisatos, *Nature* **2000**, *404*, 59 – 61.
[11] A. E. Saunders, A. Ghezelbash, P. Sood, B. A. Korgel, *Langmuir* **2008**, *24*, 9043 – 9049.
[12] S. Linic, P. Christopher, D. B. Ingram, *Nat. Mater.* **2011**, *10*, 911 – 921.
[13] A. Salant, M. Shalom, Z. Tachan, S. Buhbut, A. Zaban, U. Banin, *Nano Lett.* **2012**, *12*, 2095 – 2100.
[14] B. Weng, S. Liu, Z. R. Tang, Y. J. Xu, *RSC Adv.* **2014**, *4*, 12685 – 12700.
[15] Z. Zhang, J. T. Yates, *Chem. Rev.* **2012**, *112*, 5520 – 5551.
[16] M. Wang, F. Ren, G. Cai, Y. Liu, S. Shen, L. Guo, *Nano Res.* **2014**, *7*, 353 – 364.
[17] R. Sahoo, A. Roy, C. Ray, C. Mondal, Y. Negishi, S. M. Yusuf, A. Pal, T. Pal, *J. Phys. Chem. C* **2014**, *118*, 11485.
[18] M. M. Khan, S. A. Ansari, M. O. Ansari, B. K. Min, J. Lee, M. H. Cho, *J. Phys. Chem. C* **2014**, *118*, 9477 – 9484.
[19] M. B. Boucher, N. Yi, F. Gittleson, B. Zugic, H. Saltsburg, M. F. Stephanopoulos, *J. Phys. Chem. C* **2011**, *115*, 1261 – 1268.
[20] H. Zhu, N. Song, H. Lv, C. L. Hill, T. Lian, *J. Am. Chem. Soc.* **2012**, *134*, 11701 – 11708.
[21] W. Peng, X. Li, *Nano Res.* **2013**, *6*, 286 – 292.
[22] R. Singh, B. Pal, *J. Mol. Catal. A: Chem.* **2013**, *378*, 246 – 254.
[23] Z. Mei, S. Ouyang, D. M. Tang, T. Kako, D. Golbergc, J. Ye, *Dalton Trans.* **2013**, *42*, 2687 – 2690.
[24] S. Liu, E. Guo, L. Yin, *J. Mater. Chem.* **2012**, *22*, 5031 – 5041.
[25] F. Yang, N. N. Yan, S. Huang, Q. Sun, L. Z. Zhang, Y. Yu, *J. Phys. Chem. C* **2012**, *116*, 9078 – 9084.
[26] L. Ren, F. Yang, Y. R. Deng, N. N. Yan, S. Huang, D. Lei, Q. Sun, Y. Yu, *Int. J. Hydrogen Energy* **2010**, *35*, 3297 – 3305.
[27] Y. F. Li, D. Xu, J. I. Oh, W. Z. Shen, X. Li, Y. Yu, *ACS Catal.* **2012**, *2*, 391 – 398.
[28] T. Zuo, Z. Sun, Y. Zhao, X. Jiang, X. Gao, *J. Am. Chem. Soc.* **2010**, *132*, 6618 – 6619.
[29] M. Luo, Y. Liu, J. Hu, H. Liu, J. Li, *ACS Appl. Mater. Interfaces* **2012**, *4*, 1813 – 1821.
[30] R. Sasikala, A. R. Shirole, V. Sudarsan, K. G. Girija, R. Rao, C. Sudakarc, S. R. Bharadwaj, *J. Mater. Chem.* **2011**, *21*, 16566 – 16573.
[31] F. Zhang, X. W. He, W. Y. Li, W. K. Zhang, *J. Mater. Chem.* **2012**, *22*, 22250 – 22257.
[32] E. Khon, A. Mereshchenko, A. N. Tarnovsky, K. Acharya, A. Klinkova, N. N. Hewa-Kasakarage, I. Nemitz, M. Zamkov, *Nano Lett.* **2011**, *11*, 1792 – 1799.
[33] M. Li, X. F. Yu, S. Liang, X. N. Peng, Z. J. Yang, Y. L. Wang, Q. Q. Wang, *Adv. Funct. Mater.* **2011**, *21*, 1788 – 1794.
[34] M. Liu, L. Zhang, X. He, B. Zhang, H. Song, S. Lia, W. Youa, *J. Mater. Chem. A* **2014**, *2*, 4619 – 4626.
[35] M. Achermann, *J. Phys. Chem. Lett.* **2010**, *1*, 2837 – 2843.
[36] Q. Li, H. Meng, P. Zhou, Y. Zheng, J. Wang, J. Yu, J. Gong, *ACS Catal.* **2013**, *3*, 882 – 889.
[37] J. Zhang, Y. Wang, J. Zhang, Z. Lin, F. Huang, J. Yu, *ACS Appl. Mater. Interfaces* **2013**, *5*, 1031 – 1037.
[38] T. T. Yang, W. T. Chen, Y. J. Hsu, K. H. Wei, T. Y. Lin, T. W. Lin, *J. Phys. Chem. C* **2010**, *114*, 11414 – 11420.
[39] N. Gupta, B. Pal, *J. Colloid Interface Sci.* **2012**, *368*, 250 – 256.
[40] H. Yang, *Metals Mater. Int.* **2006**, *12*, 351 – 355.

Received: November 10, 2014
Revised: January 30, 2015
Published online on February 18, 2015